

Universal Machine Learning for the Response of Atomistic Systems to External Fields

Yaolong Zhang^{1,#} and Bin Jiang^{1,2,*}

1. *Key Laboratory of Precision and Intelligent Chemistry, Department of Chemical Physics, Key Laboratory of Surface and Interface Chemistry and Energy Catalysis of Anhui Higher Education Institutes, University of Science and Technology of China, Hefei, Anhui 230026, China*
2. *Hefei National Laboratory, University of Science and Technology of China, Hefei, 230088, China*

#: Current address: École Polytechnique Fédérale de Lausanne, 1015 Lausanne, Switzerland

*: Corresponding author: bjiangch@ustc.edu.cn

Abstract

Machine learned interatomic interaction potentials have enabled efficient and accurate molecular simulations of closed systems. However, external fields, which can greatly change the chemical structure and/or reactivity, have been seldom included in current machine learning models. This work proposes a universal field-induced recursively embedded atom neural network (FIREANN) model, which integrates a pseudo field vector-dependent feature into atomic descriptors to represent system-field interactions with rigorous rotational equivariance. This “one-for-all” approach correlates various response properties like dipole moment and polarizability with the field-dependent potential energy in a single model, very suitable for spectroscopic and dynamics simulations in both molecular and periodic systems in the presence of electric fields. Especially for periodic systems, we find that FIREANN can overcome the intrinsic multiple-value issue of the polarization by training atomic forces only. This model paves the way to efficiently modeling complicated systems in strong external fields such as electrified interfaces.

The interplay between external fields and chemical systems is of fundamental importance in a range of physical, chemical and biological processes¹. By interacting with atoms, molecules, or condensed matter, external (mainly electric) fields can induce electronic/spin polarization and spatial orientation of the system, which have offered a particular means to alter chemical structures², promote electron transfer³, control phase transitions of materials⁴ or conformational transformations of biomolecules⁵, subtly manipulate chemical reactivity and selectivity in catalysis⁶⁻⁹ and quantum dynamics in cold chemical reactions¹⁰⁻¹².

Exact field-dependent quantum scattering calculations were feasible only for very small systems¹³. Density functional theory (DFT) and ab initio molecular dynamics (AIMD) simulations based on the modern theory of polarization¹⁴ have been more commonly applied to study more complex aperiodic and periodic systems in the presence of external electric fields¹⁵⁻¹⁹. However, the AIMD approach remains very demanding, especially when nuclear quantum effects (NQEs) are important¹⁸. Although empirical force fields can be highly efficient^{20, 21}, their accuracy is limited by empirical functions and approximate polarizable models truncating the field-induced interaction to the first or second order. Moreover, they fall short to describe bond breakage/formation.

Recent years have witnessed revolutionary successes of machine learning (ML) methods in solving high-dimensional problems in chemistry²²⁻²⁸. Various ML models for accurately representing potential energy surfaces (PESs) have been developed.²⁹⁻⁴³ Some of them have been extended to learn tensorial properties such as the dipole

moment and polarizability tensor with correct rotational equivariance,⁴⁴⁻⁵³ enabling efficient field-free simulations of electronic and vibrational spectra. However, most ML models treat the potential energy and its response properties to electric fields separately, without capturing the field-dependence. The influence of electric fields was first taken into account by Christensen *et al.* in a kernel-based regression method by constructing a fictitious dipole arising from fictitious partial charges and coupling it with the field vector to yield a scalar dipole-field interaction analogue⁵⁴. Müller and coworkers incorporated the dipole-field interaction similarly in their FieldSchNet neural network (NN) model to describe the solvent effect in the form of an effective field⁵⁵. Gao and Remsing separated the long- and short-range interactions by introducing self-consistent effective electric fields, which is used as input for subsequent NNs along with local atomic coordinates to describe perturbations to the short-range system from the effective electric field. This strategy however does not rigorously fulfill the rotational equivariance with respect to the field direction⁵⁶.

In this work, by introducing a simple field-dependent feature into the description of atomic environment, we develop a field-induced recursively embedded atom neural network (FIREANN) model with correct rotational equivariance of a system interacting with an external field. Without any truncation of field-induced interactions, FIREANN describes not only the energy variation with an applied field strength and direction, but also the associated response properties simultaneously up to (in principle) any order. Path-integral based molecular dynamics simulations with well-trained FIREANN models yield reliable *ab initio* spectroscopy of representative

molecular and condensed phase systems in the presence of electric fields. A remarkable characteristic of this model is that it can detour the multivalued issue of the polarization in periodic systems, a well-known but largely neglected fact in existing ML models, by learning atomic forces only.

Results

FIREANN framework. The FIREANN model is built on top of a physics-inspired recursively embedded atom neural network (REANN) framework⁵⁷ that uses embedded atom densities (EADs) as descriptors to atomic environment (Detailed in the Methods section). In the absence of electric fields, EADs are constructed in a quantum chemical spirit by the linear combination of Gaussian-type orbitals (GTOs) of surrounding atoms, preserving the overall rotational, translational, and permutational invariance of the system. However, an applied field can certainly redistribute the electron density and break down the rotational invariance of the system. The corresponding field-system interaction depends on the direction and strength of the electric field. To characterize this influence in a physically meaningful way, for an applied field ($\vec{\epsilon}$), we include a virtual field vector-dependent function, namely,

$$\varphi_{l_x l_y l_z}(\vec{\epsilon}) = (\epsilon_x)^{l_x} (\epsilon_y)^{l_y} (\epsilon_z)^{l_z}, \quad (1)$$

leading to the following field-induced EAD (FI-EAD) feature,

$$\rho_i = \sum_{l=0}^L \sum_{l_x+l_y+l_z=l} \frac{l!}{l_x!l_y!l_z!} \left[\sum_{m=1}^{N_g} d_m \left(\sum_{j \neq i}^{N_c} c_j \varphi_{l_x l_y l_z}^m(\vec{\mathbf{r}}_{ij}) + c_\epsilon \varphi_{l_x l_y l_z}(\vec{\epsilon}_i) \right) \right]^2. \quad (2)$$

Here, the applied field felt by each atom is represented by a position vector of a pseudo-atom relative to that atom ($\vec{\epsilon}_i$), as illustrated in Fig. 1). The FI-EAD feature

can be rewritten in terms of interatomic distances and enclosed angles³⁵,

$$\begin{aligned} \rho_i = & \sum_{l=0}^L \sum_{j,k \neq i}^{N_c} c_j c_k [r_{ij} r_{ik}]^l \cos^l(\theta_{ijk}) \sum_{m,m'=1}^{N_\varphi} d_m d_{m'} f_m(r_{ij}) f_{m'}(r_{ik}) \\ & + \sum_{l=0}^L \sum_{j \neq i}^{N_c} c_j c_\varepsilon [r_{ij} \|\vec{\mathbf{e}}_i\|]^l \cos^l(\theta_{ij\varepsilon}) \sum_{m=1}^{N_\varphi} d_m f_m(r_{ij}) \end{aligned} \quad (3)$$

where we have combined the radial Gaussian and switching functions in f_m for simplicity. From Eq. (3), one immediately realizes that the FI-EAD feature depends not only on atomic coordinates, but also on the field strength ($\|\vec{\mathbf{e}}_i\|$) and the closed angle $\theta_{ij\varepsilon}$ between $\vec{\mathbf{e}}_i$ and each $\vec{\mathbf{r}}_{ij}$ vector. In practice, rotating the field or the system separately will lead to different FI-EAD values, while the synchronous rotation of the field and the system without altering the relative direction of $\vec{\mathbf{e}}$ with respect to each coordinate $\hat{\mathbf{r}}_{ij}$ will not. This FI-EAD feature captures the nature of the interaction between the system and the applied electric field without changing the physical form of the EAD feature. The resulting rotational equivariance is conserved in any subsequent message passing of the environment- and field-dependent orbital coefficients (c_j and c_ε) and thus in the final potential energy. When $\vec{\mathbf{e}}=0$, this model naturally reduces to the original REANN model.

As an extra benefit, the FIREANN framework intrinsically describes the response of the potential energy to an external field up to an arbitrary order by taking the analytical gradients of the potential energy with respect to the field vector. For example, the electric dipole moment ($\vec{\boldsymbol{\mu}}$) is the first and the polarizability tensor ($\boldsymbol{\alpha}$) the second order response to electric fields,

$$\vec{\boldsymbol{\mu}} = \sum_{i=1}^N \frac{\partial E_i}{\partial \vec{\mathbf{E}}}; \quad \boldsymbol{\alpha} = \frac{\partial \vec{\boldsymbol{\mu}}}{\partial \vec{\mathbf{E}}} = \sum_{i=1}^N \frac{\partial^2 E_i}{\partial \vec{\mathbf{E}} \partial \vec{\mathbf{E}}}. \quad (4)$$

These properties can be simultaneously learned in an FIREANN model by adopting

the following loss function,

$$\mathcal{L}(\mathbf{w}) = \sum_{m=1}^{N_b} \left[\lambda_V \times (E_m^{NN} - E_m^{Ref})^2 + \lambda_F \times \left| \left(\frac{\partial E}{\partial \mathbf{r}} \right)_m^{NN} - \vec{\mathbf{F}}_m^{Ref} \right|^2 + \lambda_\mu \times \left| \left(\frac{\partial E}{\partial \vec{\mathbf{e}}} \right)_m^{NN} - \vec{\boldsymbol{\mu}}_m^{Ref} \right|^2 + \lambda_\alpha \times \left| \left(\frac{\partial^2 E}{\partial \vec{\mathbf{e}} \partial \vec{\mathbf{e}}} \right)_m^{NN} - \boldsymbol{\alpha}_m^{Ref} \right|^2 \right] / N_b, \quad (5)$$

where N_b is the size of the batch dataset, the superscripts *NN* and *Ref* refer to the *NN*-predicted and reference quantities, and λ_V , λ_F , λ_μ and λ_α represent the weights of the energy, force, dipole moment and polarizability, respectively, in the loss function. Note that these response properties by construction offer correlated information on the field-dependence of the PES rather than being simply accumulated in the loss function³⁶. As a result, they have a similar effect as that of forces and Hessians, which can help improve the fitting quality. We also note that FIREANN not only applies to electric fields as demonstrated by numerical examples below, but also equally to magnetic fields in the same spirit, by which the magnetic dipole and/or magnetic polarizability can be obtained.

A Toy System. We first take the H₂O molecule as a toy system to verify the symmetry adaption of the FIREANN method subject to an external electric field. A FIREANN model was constructed with just a single equilibrium geometry lying in the *yz* plane and the electric field being 0.1 V/Å along the *x*-direction. As displayed in Fig. 2(a), when the molecule rotates about the *x* axis, its potential energy does not change at all as the field is always orthogonal to the molecular plane. This is exactly encoded in FIREANN. On the other hand, the potential energy varies with the molecular rotation about the *y* axis, as shown in Fig. 2(b). The energy variation representing the

interaction between the molecular dipole and the electric field is again well predicted by the FIREANN model. Importantly, FIREANN further exhibits excellent extrapolatability in Fig. 2(c), where the field intensity along the x -axis varies from -0.2 to 0.2 V/Å, resulting in a symmetrical energy dependence on the field direction. The FIREANN model trained with a single data successfully reproduces the energy profile generated by DFT. By contrast, the potential energy becomes a constant if one considers the first-order permanent dipole-field interaction only, as the permanent dipole moment always lies in the molecular plane. This is an important fact that previous ML potentials (or force fields) based on a scalar product of a virtual dipole and the field vector could fail to predict the correct field-induced energy dependence in strong electric fields^{54, 55}.

Molecular Spectroscopy. A distinct feature of the proposed FIREANN model is its one-for-all predictions for energies (atomic forces) and response properties with and without an electric field. We first demonstrate this feature for the N-methylacetamide (NMA) molecule, which has been widely used as a model system of the amide group to construct spectroscopic maps and simulate the spectra of the peptide backbone^{47, 58-61}. Specifically, we constructed an FIREANN model by learning a mix set of ab initio energies, forces, dipole moments and polarizabilities for the NMA molecule in an electric field varying from 0.0 to 0.4 V/Å along x -direction. Fig. 3 clearly shows that the universal FIREANN model achieves an excellent accuracy for energy, dipole moment, and polarizability, with corresponding root mean square errors (RMSEs) of 0.0053 eV, 0.028 Debye, and 0.51 au, respectively. Given the synchronous prediction

of these quantities, the FIREANN model enables efficient molecular dynamics (MD) simulations of IR and Raman spectra in comparison with experimental data.

Fig. 4 (a) compares the calculated and experimental field-free infrared (IR) spectra⁶² for NMA at 300 K. In general, the classical MD-based result agrees reasonably well with the experimental spectrum, even reproducing double peaks for the C-O stretching vibration ($\sim 1710 \text{ cm}^{-1}$) corresponding to the well-known P/R rotational structure induced splitting⁶². However, the calculated bands of Amide II, Amide III, Amide A (the N-H stretch band, $\sim 3507 \text{ cm}^{-1}$) and the band including C-H stretching mode and other bending overtones of the methyl group ($\sim 2950 \text{ cm}^{-1}$) are apparently blue-shifted compared to experiment. This discrepancy is likely due to the neglect of NQEs in the classical treatment of these vibrational bands relevant to hydrogen atoms. To solve this problem, path-integral based thermostated ring polymer molecular dynamics (TRPMD)⁶³ simulations were performed. The TRPMD result significantly improves the agreement with experiment and reproduces most bands in not only their positions but also their shapes and intensities. Fig 4 (b) compares the calculated and experimental resonance Raman spectra of NMA for zero field. Due to the lack of the experimental spectrum for a single NMA molecule, the measured liquid spectrum⁶⁴ is taken form qualitative comparison. Encouragingly, while there is apparent mismatch regarding the relative peak intensities of low-frequency modes, the TRPMD spectrum reproduces most of the observed bands reasonably well.

FIREANN also predicts the in-field molecular spectra, as shown in Fig. 5, where the field strength increases from 0 to 0.4 V/\AA every 0.1 V/\AA along x -direction. In

these in-field IR spectra, the C-O stretching band seems most influenced by the applied field. As mentioned in the field-free spectrum, this band has an intrinsic P/R rotational double-peak structure. Interestingly, with an increasing field strength, this P/R branch splitting gradually vanishes and the absorption peak gets narrower and higher. This phenomenon implies the interplay between the electric field and the molecular rotation. Indeed, the dipole moment of NMA, which is almost parallel to the C-O bond^{62, 65}, tends to reorient to the opposite direction of the electric field to minimize the energy. Increasing the field intensity increases the dipole-field interaction and more strongly confines the NMA molecule in the preferable orientation. In addition, a significant red shift of the CO stretching vibration is found roughly proportional to the field intensity. This red shift is likely a natural consequence of the weakening of the chemical bond by the applied electric field. A similar but smaller redshift is also found for the N-H stretching, consistent with the fact that the electron cloud of the C-O group is more polarizable than the N-H group, due apparently to the higher electron density there. Furthermore, we decompose the molecular polarizability into isotropic ($\alpha_{\text{iso}} = \text{tr}(\boldsymbol{\alpha})/3$) and anisotropic ($\boldsymbol{\alpha}_{\text{aniso}} = \boldsymbol{\alpha} - \alpha_{\text{iso}} \mathbf{I}$) terms and exhibit corresponding Raman spectra in Fig. 5, respectively. The anisotropic Raman spectra show a similar field-dependence of the C-O stretching band for the same reason. However, the rotational splitting is absent in isotropic Raman spectra as the isotropic polarizability is rotation invariant. As a result, the increasing field results in only a pure red shift of the C-O stretching vibration.

Liquid water. The FIREANN model is by its atom-wise form capable of describing

the response of periodic systems to external electric fields. However, unlike molecular systems, the polarization (dipole moment per unit volume) of a periodic system is a multivalued quantity according to the modern theory of polarization¹⁴, resulting in multiple parallel branches that differ by a polarization quantum represented by the product of any lattice vector and the electronic charge and divided by the volume of the lattice¹⁴. This ill-defined multiplicity may lead to sudden jumps of the dipole moment when atomic positions were displaced by a lattice constant due to periodicity. The accidental change of dipole moment cannot be captured by typical atomistic ML models^{44, 45, 47, 66}, if no correction was imposed, as shown in the evolution of the x -component of dipole moment along an AIMD trajectory even in the absence of an electric field (Fig. 6a). Importantly, this discontinuity issue occurs more frequently under a high field strength (Fig. 6b). Likewise, the in-field total energy is supposed to be discontinuous at these configurations as the dipole-field interaction jumps. In the FIREANN framework, fortunately, this issue can be easily bypassed by training atomic forces only in the presence of electric field, because the gradient of the energy is actually unaffected. Although the dipole moment and polarizability are not explicitly involved, the interaction between the electric field and the system can be learned implicitly in the force-only training. The dipole moment can then be retrieved by the first-order gradient of the energy output with respect to the field vector.

To validate this strategy, we have constructed a FIREANN model of bulk water including 64 water molecules under an electric field up to 0.6 V/Å along x -direction, using atomic forces as targets only (named as FIREANN-wF hereafter).

Our model yields accurate predictions for atomic forces, with an overall RMSE of 39.4 meV/Å. In addition, the TRPMD-calculated field-free radial distribution functions (RDFs) of liquid water agree very well with previous on-the-fly results at the same DFT level⁶⁷ and experimental data⁶⁸, as shown in Fig. 7, further validating the accuracy of the FIREANN-wF potential. In Fig. 6, unlike the original DFT data, the FIREANN-wF model shows a reasonably continuous variation of the dipole moment along the AIMD trajectory. Given the fact that the dipole moment should vary continuously as the configuration, it is reasonable to shift the AIMD calculated dipole moment by an integer of polarization quantum making it closest to that of the previous step. Impressively, the corrected DFT dipole moments perfectly match the FIREANN-wF predictions, without any prior knowledge on these positions of sudden jumps. Interestingly, the FIREANN-wF model captures the drastic increase of the polarization of the system under an intensive electric field, as shown in Fig. 5b. This is because of an additivity of the molecular dipole moment as each water molecule tends to align its dipole moment to the field vector. Fig. 6 also shows the poor performance of a flawed model training with multi-branched dipole moments in a brute-force way (named as FIREANN-wD hereafter), which obviously fails to follow the correct evolution of the dipole moment. Note that, although it is viable to correct the dipole moment along a single AIMD trajectory because the configuration change is minor in adjacent steps, it is difficult to do so in practice for uncorrelated trajectories or for independent single-point calculations. In latter cases, the training dataset will likely include dipole moments of unpredictable branches and give large

noises to conventional ML dipole models relying on the multiplication of atomic charges and position vectors.

Misrepresenting the dipole moment surface could have significant influence on the resultant IR spectrum. Fig. 8 (a) compares the calculated and experimental IR spectra of liquid water at room temperature without an electric field. Thanks to the inclusion of NQEs by TRPMD, the FIREANN-wF model that offers both the correct PES and dipole moment surface, does capture well all experimental vibrational features⁶⁹ including the O-H stretching ($\sim 3600 \text{ cm}^{-1}$), H-O-H bending ($\sim 1690 \text{ cm}^{-1}$), librational ($\sim 700 \text{ cm}^{-1}$)⁷⁰ and H-bonding stretching bands ($\sim 170 \text{ cm}^{-1}$)⁷⁰. Our results also agree well with previous theoretical ones obtained by on-the-fly TRPMD at the same DFT level⁶⁷, likely with their DFT dipole moments corrected. By contrast, the IR spectrum predicted by the FIREANN-wF model using the same trajectories deviates significantly from the experimental counterpart. This comparison clearly highlights the necessity of using a ML model fulfilling the physical requirement of the dipole moment in predicting IR spectra. Finally, we show in Fig. 8(b) that the predictions of the FIREANN-wF model for the IR spectrum with an electric field up to 0.4 V/\AA along x -direction. Interestingly, the electric field influences mostly the O-H stretching band, resulting in a progressive red shift upon with the increasing field intensity. Unlike the NMA molecule, the red shift here is not solely because of the softening of the O-H bond by the electric field, but also the more ordered structure as a result of the field-induced reorientation of water molecules to be parallel to the field vector¹⁹. This effect will render the liquid water structure more ice-like¹⁹, in which the

O-H vibrational band is lower in frequency. In contrast, this ordering effect hinders the librational rotation of water molecules and naturally result in an increased frequency of the librational mode. In comparison, the H-O-H bending mode is barely affected by the electric field, since the bending motion leads to little change of the direction of the dipole moment.

Discussion

In this work, we have proposed a simple, accurate, and universal FIREANN model to learn the external field-dependent PES and response properties with the proper rotational equivariance. This model allows us to obtain all ingredients from one single training for modelling spectroscopy and dynamics of chemical systems with and without external electric fields. The validity of this model is supported by the good agreement between the predicted vibrational spectra of the NMA molecule and liquid water and field-free experimental data. Moreover, the field-induced alignment of the dipole moment and the softening of the covalent bond are clearly predicted in the in-field IR or Raman spectra. For periodic systems like liquid water, in particular, the intrinsic multi-valued polarization of the system results in the discontinuous dipole moments in the training data and makes it difficult to being represented by conventional machine learning models based on atomic charges. This issue is nicely bypassed in the FIREANN model by learning atomic forces only, which can yield both field-dependent potentials and dipole moments, and thus IR spectra of liquid water. Our results not only clearly validate the high accuracy of the one-for-all FIREANN model, but also elucidate the interplay between chemical systems and

electric fields.

Although all results presented in this work are relevant to the system exposed to an electric field, the FIREANN framework can also describe the response of the system to a magnetic field or even to an electromagnetic field by introducing another field vector-dependent virtual function in Eq. (2). Note that the current version of the FIREANN model is limited to describing the influence of a homogeneous external field. In case of a non-uniform external field, the response of the electron density to the field is spatially dependent and must be explicitly considered. A feasible way is to discretize the non-uniform field to each atomic center and introduce a nonequivalent field-dependent function to each FI-EAD feature (as implicitly implied in Fig. 1) to approximate by the response of each atomic density to the local field experienced by the central atom. These desirable features make the FIREANN approach very promising to efficiently modeling strong field-induced phenomena such as electrochemistry^{71, 72}, plasmonic chemistry⁷³, and tip-induced catalytic reactions⁷.

Methods

REANN. The regular REANN model was proposed for representing field-free PESs⁵⁷. Like all atomistic NN models, the total potential energy (E) is expressed in the sum of atom-wise contributions and each atomic energy (E_i) is learned by feeding a vector of atomic features for describing the atom-centered environment to an atom-wise NN. In the REANN model, embedded atom density (EAD) atomic features are specified to include many-body correlations between the central and neighbor atoms, which are

simply evaluated by the square of the linear combination of a set of contracted Gaussian-type orbitals (GTOs) located at neighbor atoms,

$$\rho_i = \sum_{l=0}^L \sum_{l_x, l_y, l_z} \frac{l!}{l_x! l_y! l_z!} \left[\sum_{j \neq i}^{N_c} c_j \sum_{m=1}^{N_\phi} d_m \varphi_{l_x l_y l_z}^m(\vec{\mathbf{r}}_{ij}) \right]^2, \quad (6)$$

where the primitive GTO takes the following form,

$$\varphi_{l_x l_y l_z}^m(\vec{\mathbf{r}}_{ij}) = (x_{ij})^{l_x} (y_{ij})^{l_y} (z_{ij})^{l_z} \exp\left[-\alpha_m (r_{ij} - r_m)^2\right] f_c(r_{ij}). \quad (7)$$

Specifically, $\vec{\mathbf{r}}_{ij} = \vec{\mathbf{r}}_i - \vec{\mathbf{r}}_j$ is the position vector (three components) of the central atom i relative to the j th neighbor atom with $r_{ij} = (x_{ij}^2 + y_{ij}^2 + z_{ij}^2)^{1/2}$ being its norm (Cartesian component), $l = l_x + l_y + l_z$ specifies the orbital angular momentum (e.g., $l=0$ for the s orbital, $l=1$ for the p orbital, etc.), α_m and r_m are hyperparameters that determine the center and the width of the radial Gaussian function. In the combination to form an EAD feature, L is the maximum orbital angular momentum of GTOs, N_ϕ is the number of primitive GTOs for each l and d_m is the contraction coefficient of the m th primitive GTO, N_c is the number of neighbor atoms and c_j is the j th atomic orbital coefficient within a cutoff radius (r_c), $f_c(r_{ij})$ is a cosine-type switching function continuously decaying interatomic interactions to zero at r_c up to second-order derivatives. In particular, realizing that c_j itself necessarily depends on its atomic environment, we express it as the output of an atomic NN based on EAD features centered at atom j . Apparently, REANN is essentially a message-passing NN by recursively expanding the environment-dependent orbital coefficients like this, which has proven an efficient way to incorporate high-order many-body correlations in the local environment⁵⁷.

Training Details. All FIREANN models in this study utilize NN with two hidden

layers, each containing 64 neurons in each iteration of message-passing. Eight radial functions and L up to 2 were used to construct EAD features with sufficient representability. The initial learning rate was set to 0.002 and decays by a factor of 0.5 whenever the validation loss does not decrease for 100 consecutive epochs. Training stops when the learning rate drops below 1×10^{-5} . The number of message-passing iterations for H₂O, NMA, and liquid water were set to 0, 4, and 3, respectively. The cutoff distances for the three systems were 3.0 Å, 6.0 Å, and 5.0 Å. Other parameters were automatically optimized during the training process.

Computational details and datasets. Three systems are used to validate the FIREANN model, including a toy system (H₂O monomer), N-methylacetamide (NMA), and liquid water.

A Toy system. The training set of the H₂O molecule contains merely a single equilibrium geometry lying in the yz plane with an electric field of 0.1 V/Å along the x -direction. The potential energy, dipole moment and polarizability of H₂O were calculated by Gaussian 09⁷⁴ at the B3LYP/cc-pVDZ level⁷⁵ and used as targets in the loss function defined in Eq (7).

NMA. Over 13000 configurations were sampled from canonical ensemble (NVT) classical & path-integral MD simulations at 300 K in the presence of an electric field ranging from 0.0 to 0.4 V/Å along the x -direction and calculated using Gaussian 09⁷⁴ at the B3LYP/aug-cc-pVDZ level⁷⁵ with D3 correction of dispersion⁷⁶. The dataset was divided into training set, validation set and test set with a ratio of 8:1:1. Again, the potential energy, atomic force, dipole moment and polarizability were trained

simultaneously.

Liquid water. A cubic box of 64 water molecules was used in the data sampling. The dataset consists of ~33000 configurations sampled from NVT classical & path-integral AIMD simulations at 300 K with the external electric field ranging from 0.0 to 0.6 V/Å along x -direction. Electronic structures and properties were calculated by CP2K⁷⁷ with a hybrid density functional revPBE0^{78, 79} including D3 correction of dispersion⁷⁶. Goedecker–Tetter–Hutter pseudopotentials⁸⁰ with a cutoff of 1200 Ry and a TZV2P basis set were used. Only atomic forces were used to construct the PES, and the dipole moment was excluded due to its discontinuity caused by the multiple value nature of the periodic systems.

MD simulations with FIREANN models

NMA: To compare calculated IR and Raman spectra of NMA with experimental data, classical MD simulations were performed at 300 K in the absence of an electric field. The NMA molecule was first equilibrated with 20 ps using the Andersen thermostat⁸¹, after which two-hundred snapshots with corresponding momentum were randomly chosen for initializing subsequent NVE MD simulations of 25 ps. The time correlation functions (TCFs) were computed by the average of 200 such trajectories. IR and Raman spectra were obtained by the Fourier transform of the TCFs of the time derivatives of dipole and polarizability, respectively⁸². In addition, to include NQEs, path-integral based thermostated ring polymer MD (TRPMD) simulations^{63, 83} were performed with Langevin thermostats attached to all non-centroid normal modes, with and without adding an electric field. Other computational details are similar to those

in the classical MD simulations. The resulting field-dependent IR and Raman spectra were obtained by the Fourier transform of the centroid-based TCFs on average of 200 TRPMD trajectories. In all simulations, the time step was kept at 0.1 fs.

Liquid water: The system consists of 64 H₂O molecules with its side length 12.4185 Å. The NVT classical MD simulations of liquid water were performed at 300 K, using Andersen thermostat⁸¹. To obtain convergent IR spectra, we extracted 128 positions and momentum from an equilibrium NVT trajectory as initial states for NVE MD simulations, with a total time of 20 ps per NVE simulation and a time step of 0.1 fs. The same setup was used for a 24-bead TRPMD simulations to include NQEs, which was found to converge the spectroscopic results.

Data availability:

The dataset of NMA molecules and liquid water will be made publicly available upon acceptance of the manuscript.

Code availability:

The FIREANN package will be made publicly available upon acceptance of the manuscript.

Reference

1. SHAIK SS, STUYVER T. *Effects of electric fields on structure and reactivity: new horizons in chemistry*. The Royal Society of Chemistry (2021).
2. Alemani M, Peters MV, Hecht S, Rieder K-H, Moresco F, Grill L. Electric Field-Induced Isomerization of Azobenzene by STM. *J Am Chem Soc* **128**, 14446-14447 (2006).
3. Murgida DH, Hildebrandt P. Electron-Transfer Processes of Cytochrome c at Interfaces. New Insights by Surface-Enhanced Resonance Raman Spectroscopy. *Acc Chem Res* **37**, 854-861 (2004).
4. Velpula G, Teyssandier J, De Feyter S, Mali KS. Nanoscale Control over the Mixing Behavior of Surface-Confined Bicomponent Supramolecular Networks Using an

- Oriented External Electric Field. *ACS Nano* **11**, 10903-10913 (2017).
5. English NJ, Mooney DA. Denaturation of hen egg white lysozyme in electromagnetic fields: A molecular dynamics study. *J Chem Phys* **126**, 091105 (2007).
 6. Shaik S, Mandal D, Ramanan R. Oriented electric fields as future smart reagents in chemistry. *Nat Chem* **8**, 1091-1098 (2016).
 7. Ciampi S, Darwish N, Aitken HM, Díez-Pérez I, Coote ML. Harnessing electrostatic catalysis in single molecule, electrochemical and chemical systems: a rapidly growing experimental tool box. *Chem Soc Rev* **47**, 5146-5164 (2018).
 8. Shaik S, Ramanan R, Danovich D, Mandal D. Structure and reactivity/selectivity control by oriented-external electric fields. *Chem Soc Rev* **47**, 5125-5145 (2018).
 9. Aragonès AC, *et al.* Electrostatic catalysis of a Diels–Alder reaction. *Nature* **531**, 88-91 (2016).
 10. Friedrich B, Herschbach DR. Spatial orientation of molecules in strong electric fields and evidence of pendular states. *Nature* **353**, 412 (1991).
 11. Sussman BJ, Townsend D, Ivanov MY, Stolow A. Dynamic Stark Control of Photochemical Processes. *Science* **314**, 278-281 (2006).
 12. de Miranda MHG, *et al.* Controlling the quantum stereodynamics of ultracold bimolecular reactions. *Nat Phys* **7**, 502-507 (2011).
 13. Tscherbul TV, Krems RV. Tuning Bimolecular Chemical Reactions by Electric Fields. *Phys Rev Lett* **115**, 023201 (2015).
 14. King-Smith RD, Vanderbilt D. Theory of polarization of crystalline solids. *Phys Rev B* **47**, 1651-1654 (1993).
 15. Meir R, Chen H, Lai W, Shaik S. Oriented Electric Fields Accelerate Diels–Alder Reactions and Control the endo/exo Selectivity. *ChemPhysChem* **11**, 301-310 (2010).
 16. Zhang C, Sprik M. Finite field methods for the supercell modeling of charged insulator/electrolyte interfaces. *Phys Rev B* **94**, 245309 (2016).
 17. Saitta AM, Saija F, Giaquinta PV. Ab Initio Molecular Dynamics Study of Dissociation of Water under an Electric Field. *Phys Rev Lett* **108**, 207801 (2012).
 18. Cassone G. Nuclear Quantum Effects Largely Influence Molecular Dissociation and Proton Transfer in Liquid Water under an Electric Field. *J Phys Chem Lett* **11**, 8983-8988 (2020).
 19. Cassone G, Sponer J, Trusso S, Saija F. Ab initio spectroscopy of water under electric fields. *Phys Chem Chem Phys* **21**, 21205-21212 (2019).
 20. Vegiri A, Schevkunov SV. A molecular dynamics study of structural transitions in small water clusters in the presence of an external electric field. *J Chem Phys* **115**, 4175-4185 (2001).
 21. Acosta-Gutiérrez S, Hernández-Rojas J, Bretón J, Llorente JMG, Wales DJ. Physical properties of small water clusters in low and moderate electric fields. *J Chem Phys* **135**, 124303 (2011).
 22. Musil F, Grisafi A, Bartók AP, Ortner C, Csányi G, Ceriotti M. Physics-Inspired Structural Representations for Molecules and Materials. *Chem Rev* **121**, 9759-9815 (2021).
 23. Unke OT, *et al.* Machine Learning Force Fields. *Chem Rev* **121**, 10142-10186 (2021).
 24. Behler J. Four Generations of High-Dimensional Neural Network Potentials. *Chem Rev* **121**, 10037-10072 (2021).

25. Kang P-L, Shang C, Liu Z-P. Large-Scale Atomic Simulation via Machine Learning Potentials Constructed by Global Potential Energy Surface Exploration. *Acc Chem Res* **53**, 2119-2129 (2020).
26. Huang B, von Lilienfeld OA. Ab Initio Machine Learning in Chemical Compound Space. *Chem Rev* **121**, 10001-10036 (2021).
27. Deringer VL, Bartók AP, Bernstein N, Wilkins DM, Ceriotti M, Csányi G. Gaussian Process Regression for Materials and Molecules. *Chem Rev* **121**, 10073-10141 (2021).
28. Zhang Y, Lin Q, Jiang B. Atomistic neural network representations for chemical dynamics simulations of molecular, condensed phase, and interfacial systems: Efficiency, representability, and generalization. *WIREs Comput Mol Sci* **n/a**, e1645 (2023).
29. Behler J, Parrinello M. Generalized neural-network representation of high-dimensional potential-energy surfaces. *Phys Rev Lett* **98**, 146401 (2007).
30. Bartók AP, Payne MC, Kondor R, Csányi G. Gaussian approximation potentials: The accuracy of quantum mechanics, without the electrons. *Phys Rev Lett* **104**, 136403 (2010).
31. Jiang B, Guo H. Permutation invariant polynomial neural network approach to fitting potential energy surfaces. *J Chem Phys* **139**, 054112 (2013).
32. Shao K, Chen J, Zhao Z, Zhang DH. Communication: Fitting potential energy surfaces with fundamental invariant neural network. *J Chem Phys* **145**, 071101 (2016).
33. Schütt KT, Sauceda HE, Kindermans P-J, Tkatchenko A, Müller K-R. SchNet – A deep learning architecture for molecules and materials. *J Chem Phys* **148**, 241722 (2018).
34. Zhang L, Han J, Wang H, Car R, E W. Deep Potential Molecular Dynamics: A Scalable Model with the Accuracy of Quantum Mechanics. *Phys Rev Lett* **120**, 143001 (2018).
35. Zhang Y, Hu C, Jiang B. Embedded atom neural network potentials: Efficient and accurate machine learning with a physically inspired representation. *J Phys Chem Lett* **10**, 4962-4967 (2019).
36. Unke OT, Meuwly M. PhysNet: A Neural Network for Predicting Energies, Forces, Dipole Moments, and Partial Charges. *J Chem Theory Comput* **15**, 3678-3693 (2019).
37. Zaverkin V, Kästner J. Gaussian Moments as Physically Inspired Molecular Descriptors for Accurate and Scalable Machine Learning Potentials. *J Chem Theory Comput* **16**, 5410-5421 (2020).
38. Shapeev AV. Moment Tensor Potentials: A Class of Systematically Improvable Interatomic Potentials. *Multiscale Model Sim* **14**, 1153-1173 (2016).
39. Zubatyuk R, Smith Justin S, Leszczynski J, Isayev O. Accurate and transferable multitask prediction of chemical properties with an atoms-in-molecules neural network. *Sci Adv* **5**, eaav6490 (2021).
40. Unke OT, Chmiela S, Gastegger M, Schütt KT, Sauceda HE, Müller K-R. SpookyNet: Learning force fields with electronic degrees of freedom and nonlocal effects. *Nat Commun* **12**, 7273 (2021).
41. Sauceda HE, Gálvez-González LE, Chmiela S, Paz-Borbón LO, Müller K-R, Tkatchenko A. BIGDML—Towards accurate quantum machine learning force fields for materials. *Nat Commun* **13**, 3733 (2022).
42. Braams BJ, Bowman JM. Permutationally invariant potential energy surfaces in high dimensionality. *Int Rev Phys Chem* **28**, 577-606 (2009).

43. Dral PO, *et al.* MLatom 2: An Integrative Platform for Atomistic Machine Learning. *Top Curr Chem* **379**, 27 (2021).
44. Gastegger M, Behler J, Marquetand P. Machine learning molecular dynamics for the simulation of infrared spectra. *Chem Sci* **8**, 6924-6935 (2017).
45. Grisafi A, Wilkins DM, Csányi G, Ceriotti M. Symmetry-adapted machine learning for tensorial properties of atomistic systems. *Phys Rev Lett* **120**, 036002 (2018).
46. Zhang Y, Maurer RJ, Jiang B. Symmetry-Adapted High Dimensional Neural Network Representation of Electronic Friction Tensor of Adsorbates on Metals. *J Phys Chem C* **124**, 186-195 (2020).
47. Zhang Y, Ye S, Zhang J, Hu C, Jiang J, Jiang B. Efficient and Accurate Simulations of Vibrational and Electronic Spectra with Symmetry-Preserving Neural Network Models for Tensorial Properties. *J Phys Chem B* **124**, 7284-7290 (2020).
48. Schütt K, Unke O, Gastegger M. Equivariant message passing for the prediction of tensorial properties and molecular spectra. In: *Proceedings of the 38th International Conference on Machine Learning* (eds Marina M, Tong Z). PMLR (2021).
49. Nigam J, Willatt MJ, Ceriotti M. Equivariant representations for molecular Hamiltonians and N-center atomic-scale properties. *J Chem Phys* **156**, 014115 (2021).
50. Westermayr J, Gastegger M, Marquetand P. Combining SchNet and SHARC: The SchNarc Machine Learning Approach for Excited-State Dynamics. *J Phys Chem Lett* **11**, 3828-3834 (2020).
51. Sommers GM, Calegari Andrade MF, Zhang L, Wang H, Car R. Raman spectrum and polarizability of liquid water from deep neural networks. *Phys Chem Chem Phys* **22**, 10592-10602 (2020).
52. Huang X, Braams BJ, Bowman JM. Ab initio potential energy and dipole moment surfaces for H₃O₂⁺. *J Chem Phys* **122**, 044308 (2005).
53. Medders GR, Paesani F. Infrared and Raman Spectroscopy of Liquid Water through "First-Principles" Many-Body Molecular Dynamics. *J Chem Theory Comput* **11**, 1145-1154 (2015).
54. Christensen AS, Faber FA, Lilienfeld OAv. Operators in quantum machine learning: Response properties in chemical space. *J Chem Phys* **150**, 064105 (2019).
55. Gastegger M, Schütt KT, Müller K-R. Machine learning of solvent effects on molecular spectra and reactions. *Chem Sci* **12**, 11473-11483 (2021).
56. Gao A, Rensing RC. Self-consistent determination of long-range electrostatics in neural network potentials. *Nat Commun* **13**, 1572 (2022).
57. Zhang Y, Xia J, Jiang B. Physically Motivated Recursively Embedded Atom Neural Networks: Incorporating Local Completeness and Nonlocality. *Phys Rev Lett* **127**, 156002 (2021).
58. Wang L, Middleton CT, Zanni MT, Skinner JL. Development and Validation of Transferable Amide I Vibrational Frequency Maps for Peptides. *J Phys Chem B* **115**, 3713-3724 (2011).
59. Ye S, *et al.* A neural network protocol for electronic excitations of *N*-methylacetamide. *Proc Natl Acad Sci USA* **116**, 11612-11617 (2019).
60. Zhang J, *et al.* A Machine-Learning Protocol for Ultraviolet Protein-Backbone Absorption Spectroscopy under Environmental Fluctuations. *J Phys Chem B* **125**, 6171-

- 6178 (2021).
61. Zhao L, *et al.* Accurate Machine Learning Prediction of Protein Circular Dichroism Spectra with Embedded Density Descriptors. *JACS Au* **1**, 2377-2384 (2021).
 62. Forsting T, Gottschalk HC, Hartwig B, Mons M, Suhm MA. Correcting the record: the dimers and trimers of trans-N-methylacetamide. *Phys Chem Chem Phys* **19**, 10727-10737 (2017).
 63. Rossi M, Ceriotti M, Manolopoulos DE. How to remove the spurious resonances from ring polymer molecular dynamics. *J Chem Phys* **140**, 234116 (2014).
 64. Herrebout WA, Clou K, Desseyn HO. Vibrational Spectroscopy of N-Methylacetamide Revisited. *J Phys Chem A* **105**, 4865-4881 (2001).
 65. Zhang Y, Jiang J, Jiang B. Chapter 19 - Learning dipole moments and polarizabilities. In: *Quantum Chemistry in the Age of Machine Learning* (ed Dral PO). Elsevier (2023).
 66. Zhang L, Chen M, Wu X, Wang H, E W, Car R. Deep neural network for the dielectric response of insulators. *Phys Rev B* **102**, 041121 (2020).
 67. Marsalek O, Markland TE. Quantum Dynamics and Spectroscopy of Ab Initio Liquid Water: The Interplay of Nuclear and Electronic Quantum Effects. *J Phys Chem Lett* **8**, 1545-1551 (2017).
 68. Soper AK. The radial distribution functions of water and ice from 220 to 673 K and at pressures up to 400 MPa. *Chem Phys* **258**, 121-137 (2000).
 69. Bertie JE, Lan Z. Infrared Intensities of Liquids XX: The Intensity of the OH Stretching Band of Liquid Water Revisited, and the Best Current Values of the Optical Constants of H₂O(l) at 25°C between 15,000 and 1 cm⁻¹. *Appl Spectrosc* **50**, 1047-1057 (1996).
 70. Silvestrelli PL, Bernasconi M, Parrinello M. Ab initio infrared spectrum of liquid water. *Chem Phys Lett* **277**, 478-482 (1997).
 71. Groß A. Challenges in the modeling of elementary steps in electrocatalysis. *Curr Opin Electrochem* **37**, 101170 (2023).
 72. Rossmeisl J, Nørskov JK, Taylor CD, Janik MJ, Neurock M. Calculated Phase Diagrams for the Electrochemical Oxidation and Reduction of Water over Pt(111). *J Phys Chem B* **110**, 21833-21839 (2006).
 73. Seemala B, *et al.* Plasmon-Mediated Catalytic O₂ Dissociation on Ag Nanostructures: Hot Electrons or Near Fields? *ACS Energy Letters* **4**, 1803-1809 (2019).
 74. Frisch MJ, *et al.* Gaussian 09 Revision B.01. Gaussian Inc. (2009).
 75. Becke AD. Density-functional exchange-energy approximation with correct asymptotic behavior. *Phys Rev A* **38**, 3098 (1988).
 76. Grimme S, Antony J, Ehrlich S, Krieg H. A consistent and accurate ab initio parametrization of density functional dispersion correction (DFT-D) for the 94 elements H-Pu. *J Chem Phys* **132**, 154104 (2010).
 77. Kühne TD, *et al.* CP2K: An electronic structure and molecular dynamics software package - Quickstep: Efficient and accurate electronic structure calculations. *J Chem Phys* **152**, 194103 (2020).
 78. Adamo C, Barone V. Toward reliable density functional methods without adjustable parameters: The PBE0 model. *J Chem Phys* **110**, 6158-6170 (1999).
 79. Goerigk L, Grimme S. A thorough benchmark of density functional methods for general

- main group thermochemistry, kinetics, and noncovalent interactions. *Phys Chem Chem Phys* **13**, 6670-6688 (2011).
80. Goedecker S, Teter M, Hutter J. Separable dual-space Gaussian pseudopotentials. *Phys Rev B* **54**, 1703-1710 (1996).
 81. Andersen HC. Molecular dynamics simulations at constant pressure and/or temperature. *J Chem Phys* **72**, 2384-2393 (1980).
 82. Thomas M, Brehm M, Fligg R, Vohringer P, Kirchner B. Computing vibrational spectra from ab initio molecular dynamics. *Phys Chem Chem Phys* **15**, 6608-6622 (2013).
 83. Craig IR, Manolopoulos DE. Quantum statistics and classical mechanics: Real time correlation function from ring polymer molecular dynamics. *J Chem Phys* **121**, 3368-3373 (2004).

Acknowledgement:

This work is supported by the Strategic Priority Research Program of the Chinese Academy of Sciences (XDB0450101), Innovation Program for Quantum Science and Technology (2021ZD0303301), CAS Project for Young Scientists in Basic Research (YSBR-005), National Natural Science Foundation of China (22221003 and 22033007). We acknowledge the Supercomputing Center of USTC, Hefei Advanced Computing Center, Beijing PARATERA Tech CO., Ltd for providing high-performance computing service. We also thank Dr. Wei Hu, Dr. Mouyi Weng and Junfeng Qiao for very helpful discussion.

Author contributions

B.J. designed the project, Y.Z. and B.J. discussed the neural network architecture. Y.Z. wrote the code and performed all calculations. Y.Z. and B.J. wrote the manuscript.

Competing interests

The authors declare no competing interests.

Additional information

There is no other additional information.

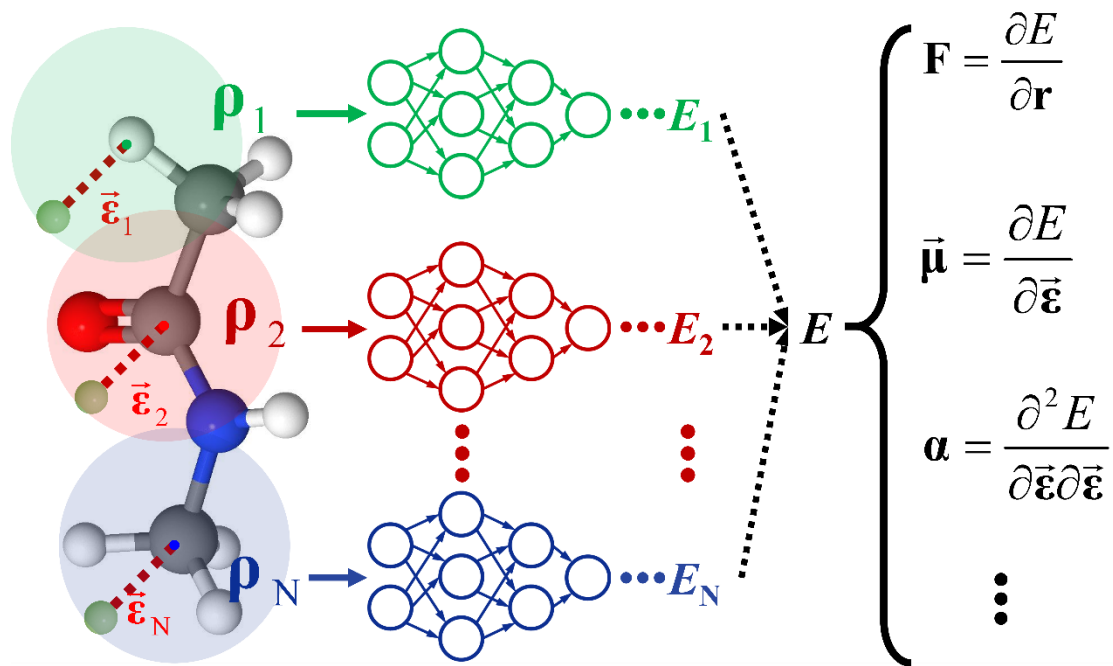


Fig. 1: Schematic of FIREANN framework. The FIREANN framework introduces a pseudo atomic field vector relative to each atom (represented by the green transparent atom) on top of standard atomistic neural network, yielding the field-dependent energy and its derivatives with respect to the field.

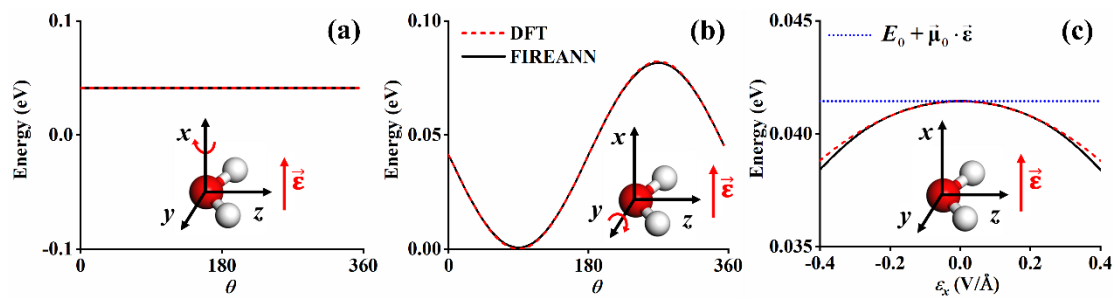


Fig. 2. Rotational and field intensity dependence of the FIREANN model.

Comparison of energy curves of a water molecule rotating about the (a) x axis and (b) y axis calculated by DFT and FIREANN, where an electric field with the intensity of 0.1 V/Å is applied along the x axis; (c) DFT and FIREANN energy curves varying with the electric field intensity, compared with that approximated by the first-order dipole-field interaction.

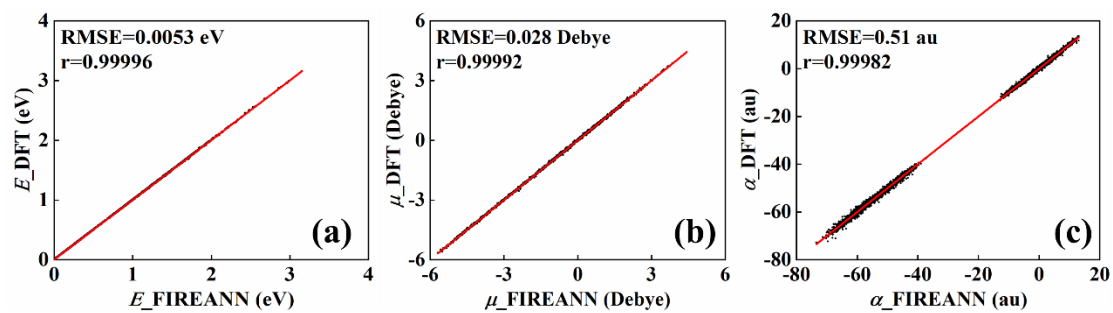


Fig. 3. Performance of the FIREANN model for NMA. Correlation plots of (a) potential energies, (b) dipole moments, and (c) polarizabilities based on FIREANN predictions and DFT data in the test set.

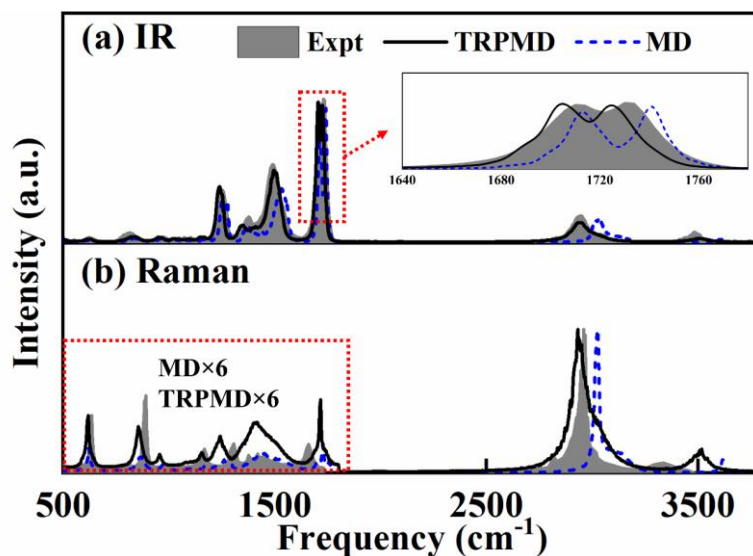


Fig. 4 Field-free vibrational spectra of NMA. Comparison of experimental, MD- and TRPMD-based (a) IR and (b) Raman spectra of the NMA molecule at 300 K. In panel (a) the inset zooms in the C-O stretching vibration peak around 1700 cm^{-1} to show the P/R rotation branches more clearly. In panel (b) the intensity of the calculated Raman spectra in the low-frequency region is amplified by a factor of 6 for qualitative comparison with the measured liquid spectrum⁶⁴ due to the lack of the experimental spectrum for a single NMA molecule.

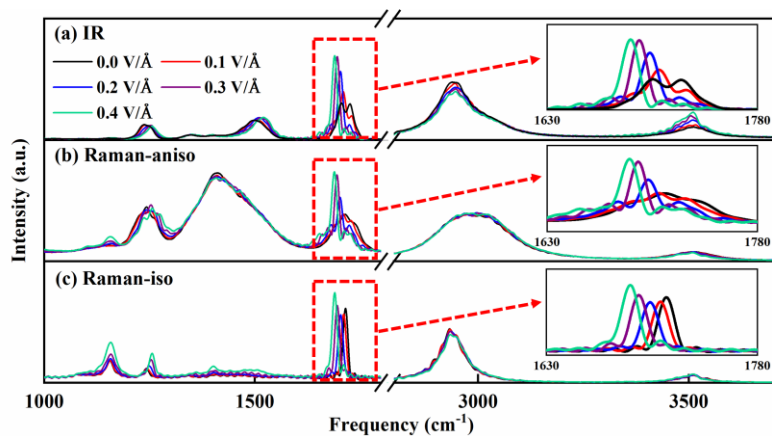


Fig. 5 In-field vibrational spectra predicted by FIREANN. Comparison of TRPMD based (a) IR, (b) Raman anisotropic and (c) Raman isotropic spectra of NMA at 300 K varying with the external electric field intensity. The inset in each panel zooms in the corresponding C-O stretching vibration peaks. Note that the high-frequency bands above 2800 cm^{-1} in panels (a), (b), and (c) are multiplied by a factor of 10, 0.1 and 0.05 for show the peaks in a similar scale.

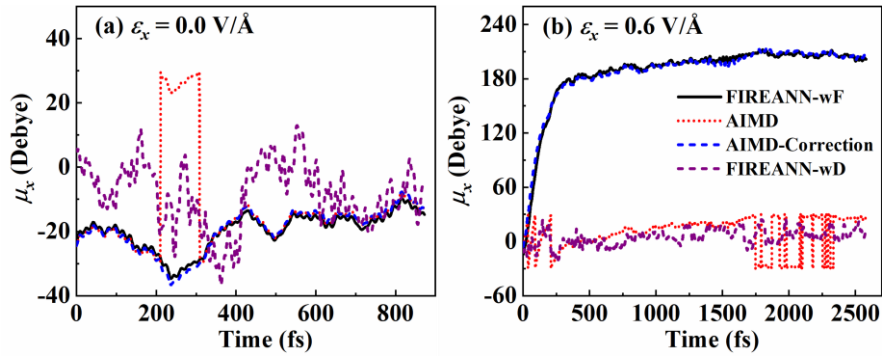


Fig. 6 Multi-valued dipole-moments in liquid water. Comparison of x component of dipole moments calculated by the FIREANN-wF and FIREANN-wD models with DFT data along the AIMD trajectory as a function of time, for (a) zero field and (b) an electric field ($\epsilon_x=0.6 \text{ V/\AA}$) along x direction. Note that the FIREANN-wF predicted dipole moment, which is deduced by the energy gradient to the electric field vector introduces an undetermined constant factor, is shifted by a constant to match the DFT value.

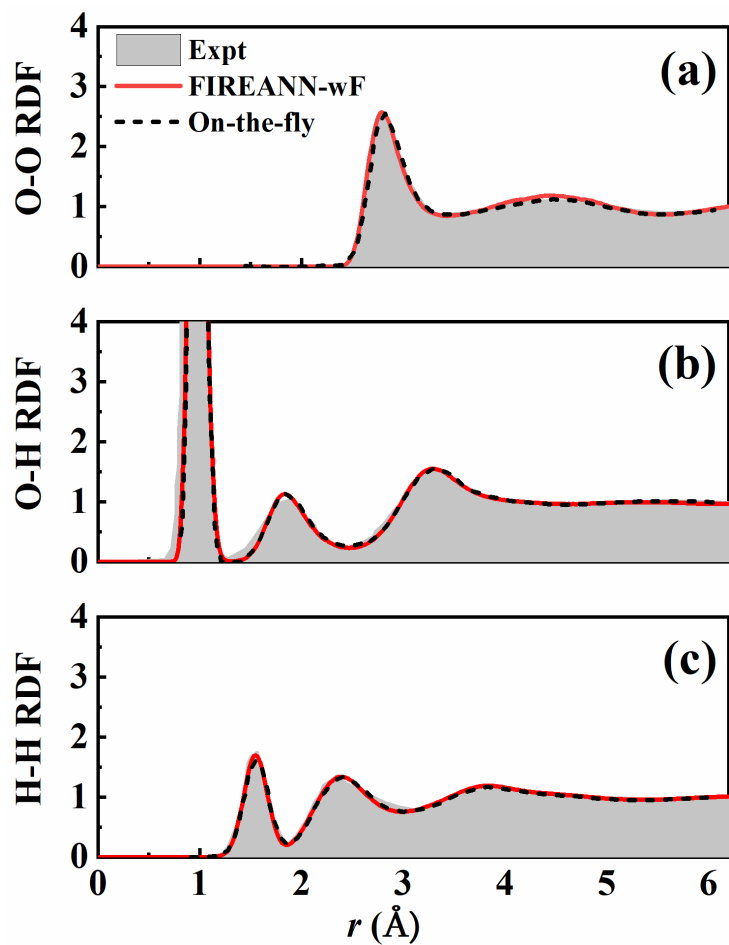


Fig. 7. Radial distribution functions of liquid water. Comparison of the experimental⁶⁸ and theoretical (a) O-O RDF, (b) O-H RDF and H-H RDF for liquid water at 300 K. Theoretical results are based on TRPMD simulations with the FIREANN PES or with on-the-fly DFT calculations extracted from Ref. ⁶⁷.

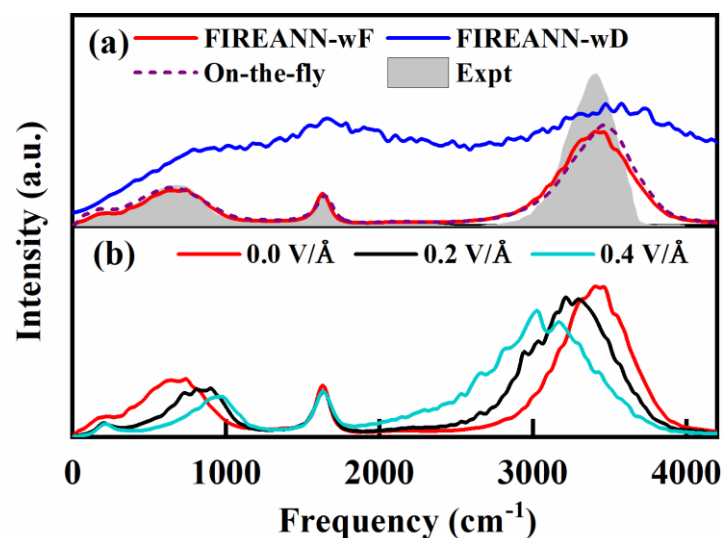


Fig. 8 Field-free and in-field IR spectra of liquid water. (a) Comparison of experimental⁶⁹ (gray) and three TRPMD-based IR spectra of liquid water in the absence of electric field at 300 K, computed with FIREANN-wF (red) and FIREANN-wD (blue) models, and on-the-fly DFT extracted from Ref. ⁶⁷ (purple). (b) Comparison of TRPMD-based IR spectra of liquid water obtained from the FIREANN-wF model with electric fields of 0.0 V/Å (red), 0.2 V/Å (black), and 0.4 V/Å (cyan) along the x -direction.